ICAS 2021 SHANG HAI
International Council of the Aeronautical Sciences
32nd Congress of the International Council of the Aeronautical Sciences
September 6-10, 2021
Pudong Shangri-La, Shanghai, China

STUDY ON THE STATISTICAL CHARACTERISTICS OF SKIN FRICTION OF SHOCK WAVE/ TURBULENT BOUDARY LAYER INTERATION IN A HOLLOW FLARE CONFIGURATION AT MACH 6

Pengfei Shen[1], Hengyu Cai[3], Pengxin Liu[1], Dong Sun[1], Xianxu Yuan[1,2,*]

[1]State Key Laboratory of Aerodynamics. Mianyang Sichuan 621000, China

[2]Computational Aerodynamics Institute, China Aerodynamics Research & Development Center, Miangyang Sichuan 621000, China

[3]School of Aeronautics, Northwestern Polytechnical University, Xi'an, Shanxi 710072, China

Abstract

Shock Wave/turbulent Boundary layer Interaction (SWTBLI) is common on the surfaces of current hypersonic vehicles with strong nonlinear effect on turbulent boundary layer. The present work mainly focuses on the skin friction of SWBTLI in a hollow cylinder-flare configuration at Mach 6 using direct numerical simulation. The exact structures of coherent vortices and statistical properties have been obtained. On the basis of the flowfield data, the formula of decomposition into 5 parts: convection, turbulent dissipation, viscous dissipation, streamwise heterogeneous quality and extra part due to coordinate system transformation using the formula. Moreover, to study the unsteady properties of the flowfield, the proper orthogonal decomposition method was used to decompose the pressure pulsation. POD results indicate that modes coefficients obeys the normal distribution mainly, and mode energy increase with modes increase.

Keywords: Shock Wave/turbulent Boundary layer Interaction; Unsteady flow; Direct numerical simulation; skin friction decomposition; Proper orthogonal decomposition

1. Introduction

Shock Wave/turbulent Boundary layer Interaction is a common phenomenon which is with strong nonlinear effect on turbulent boundary layer. Since Ferry[1] found the phenomenon and study the reason, theoretical analysis method, numerical simulation and experiment measures have been used to resolve the secrets. But until today, the problem hasn't been resolved fully. The reason is that the complexity of flow makes it difficult for existing numerical simulation methods and experimental observation method to fully capture all the details of flow, and the other is that various physical mechanics (shock interaction, flow separation, unsteady effect and compressible effect et al.)make it difficult to determine the physical phenomenon of mathematical models.

In order to study the problem, in recent years, a large number of researchers have applied high-precision numerical schemes and accurate observation measures in the three-dimensional effect of shock wave/boundary layer interaction, low frequency oscillation, flow separation effect and unsteady characteristics. About experiments, Bookey[2] et al. carried out experimental studies on oblique shock wave reflection SWBTLI and found that there are obvious differences in the direction of the exhibition, in addition to, the 'Owl eye' structure is also found in the separation zone. In the relevant numerical simulation research, Sun Dong et al.[3] studied the oscillation mechanism and found that the extended oscillation mechanism has a greater impact on the flow chararcteristics near the wall and leads to a decrease in the proportion of low frequency energy while a significant increase in the strength of Gortler vortex structures have been existed.

Local high skin friction/heat peaks on the surface of aircraft due to interaction from the turbulent boundary layer are important issues in engineering. In order to analyze the internal mechanism of skin friction, a large of researchers have carried out in-depth research in the field. Fukagata, Iwanmoto et al.[4] obtained a skin friction decomposition method called FIK definition by

simultaneously three order integral on both sided of the incompressible Reynolds average momentum equation. Renard & Deck et al.[5] have taken a different approach to solve the problem and obtained a different way of skin friction decomposition compared to FIK, known as RD skin friction decomposition formula. Sung et al.[6] used Yoon et al.[7] friction skin friction formula to study the use of large scale structure of the outer region of the incompressible turbulent plate boundary layer and pointed out that the vortex-velocity correlation is closely related to convection transport and vortex stretching within the boundary layer, and the growth of the induced skin friction generation.

In general, the existing direct numerical simulation of shock wave/boundary layer interaction is mainly in simple form, and the study of skin friction peak and heat flow peak's mechanism is not in-depth, but only in the qualitative analysis. A combination of the two configuration is even rarer. From the point of view of the nature of physics, there is a close relationship between skin friction and flow structure, so it is necessary to study skin friction with studying coherent structure.

The work of this paper is organized as follows. Section 2 describes the numerical methods and grid of the configuration. Section 3 presents the present results about instant and averaged flowfield. In section 4, the skin friction formula under the column coordinate system, and accuracy of the theory that the decomposition results have been verified, and the unsteady characteristics of skin friction using proper orthogonal decomposition is discussed in section 5. And some conclusions are drawn in the last section.

2. Computational strategy

The specific shape is computed as a three-dimensional cylinder-flare with an angle of 8.5 degrees between the cylinder and the flare. Figure 1 shows the sketch map of cylinder-flare configuration. In figure 1, the radius of the cylinder r_0 is 137mm while the computing domain normal height is 40mm, and the total streamwise length l is about 450mm, of which the cylindrical length l_0 is 375mm. The spanwise arc is 0.2 and the spanwise length of the cylindrical surface is 28mm. Figure 2 shows the exact locations of sample points and the grid mesh. The number of grids is set as three directions: streamwise 1650, normal 319 and spanwise 280. The meshes are fitted with the surface of the aircrafts which is orthogonal near the compression corner, while meshes in the other area are distributed exponentially along the bottom-to top boundary. To increase the memory of calculating process, five sample points are setted which are located at incoming turbulent layer zone, intermittent zone, interaction zone, reattachment zone and the zone after reattachment.

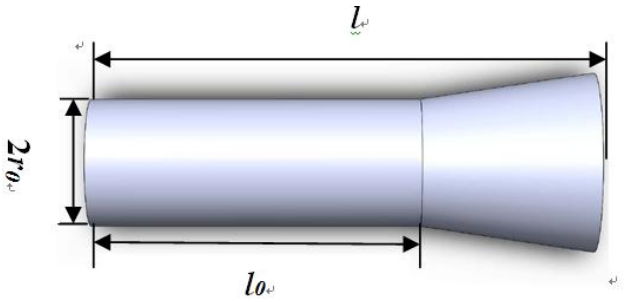

Figure 1 The sketch map of cylinder-flare configuration

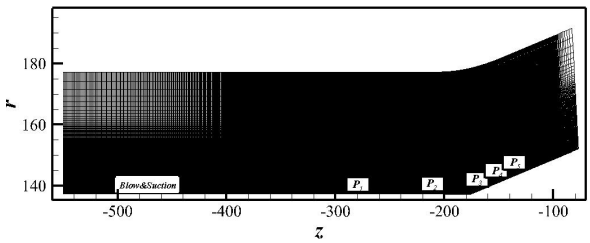

Figure 2 The grid mesh of computing domain and sample points distribution

A three-dimensional compressible Navier-Stokes conservation equations in curvilinear coordinate form are employed in present simulation. The specific form of the control equations is:

$$\frac{\partial}{\partial t}\vec{U}+\frac{\partial}{\partial x}\vec{f_1}+\frac{\partial}{\partial r}\vec{f_2}+\frac{\partial}{\partial \theta}\vec{f_3}+\vec{E_i}=\left(\frac{\partial}{\partial t}\vec{V}+\frac{\partial}{\partial x}\vec{V_1}+\frac{\partial}{\partial r}\vec{V_2}+\frac{\partial}{\partial \theta}\vec{V_3}+\vec{E_v}\right) \tag{1}$$

Where the items in (1) is:

$$
\begin{aligned}
\overrightarrow{U} &= r\left[\rho, \rho u, \rho v, \rho w, E\right]^T \\
\overrightarrow{f_1} &= r\left[\rho u, \rho u^2 + p, \rho uv, \rho uw, u\left(E+p\right)\right]^T \\
\overrightarrow{f_2} &= r\left[\rho v, \rho vu, \rho v^2 + p, \rho vw, v\left(E+p\right)\right]^T \\
\overrightarrow{f_3} &= \left[\rho w, \rho wu, \rho wv, \rho w^2 + p, w\left(E+p\right)\right]^T \\
\overrightarrow{E_i} &= \left[0, 0, -\rho w^2 - p, -\rho vw, 0\right]^T \\
\overrightarrow{V_1} &= r\left[0, \sigma_{11}, \sigma_{12}, \sigma_{13}, u\sigma_{11} + v\sigma_{12} + w\sigma_{13} + \frac{C_p \mu}{\mathrm{Pr}} \frac{\partial T}{\partial x}\right]^T \\
\overrightarrow{V_2} &= r\left[0, \sigma_{21}, \sigma_{22}, \sigma_{23}, u\sigma_{21} + v\sigma_{22} + w\sigma_{23} + \frac{C_p \mu}{\mathrm{Pr}} \frac{\partial T}{\partial r}\right]^T \\
\overrightarrow{V_3} &= \left[0, \sigma_{31}, \sigma_{32}, \sigma_{33}, u\sigma_{31} + v\sigma_{32} + w\sigma_{33} + \frac{C_p \mu}{\mathrm{Pr}} \frac{\partial T}{\partial \theta}\right]^T \\
\overrightarrow{E_v} &= \left[0, 0, -\sigma_{33}, \sigma_{23}, 0\right]^T
\end{aligned}
\tag{2}
$$

In (2), $\overrightarrow{U}$ stands for conservation properties, $\overrightarrow{f_1}$, $\overrightarrow{f_2}$, $\overrightarrow{f_3}$ stands for Eulerian fluxes, $\overrightarrow{V_1}$, $\overrightarrow{V_2}$, $\overrightarrow{V_3}$ stands for viscious fluxes. Futhermore, σ_{ij} is the vicious stress tensor which satisfies with the following relationship:

$$\sigma_{ij} = 2\mu S_{ij} - \frac{2}{3}\mu S_{kk}\delta_{ij} \tag{3}$$

And $S_{ij} = \left(u_{i,j} + u_{j,i}\right)/2$. The molecular viscosity is assumed to obey Sutherland's law while thermal conductivity meets the relationship $\kappa = C_p \mu / \mathrm{Pr}$ where κ is 0.72 u in a general way.

And in the paper, opencfd-SC high-precision differential solver is used to simulate the control equation numerically, and its calculation accuracy and program reliability are verified by a large of number of studies[8]. The Eulerian fluxes are discretized by means of a optimized sixth-order monotonicity-preserving scheme[9] by nonlinear spectral analysis with steger-warming splitting. The viscous items are discretized by a sixth-order centeral differential scheme, and the time intergration scheme is performed by means of a third-order TVD Runge-Kutta method. Adaptive filtering has been added near shock wave to maintain computational robustness.

About boundary condition, homogeneous Neumann boundary conditions for temperature and pressure are specified at the no-slip smooth wall as the same as homogeneous Dirichlet boundary conditions for the velocity components at lower boundary of the domain. And nonreflecting boundary condistion are enforced at the putlet of the domain. To trigger the transition from laminar flow to turbulent flow, the blow and the suction for velocity is used to induce the process. And the formula of blow and suction could be written as the following form:

$$
\begin{aligned}
v_{in} &= Ag\left(w_g \theta\right)\frac{4}{\sqrt{27}}\sin\left(\varphi_x\right)\left(1-\cos\left(\varphi_x\right)\right) \\
\varphi_x &= 2\pi\left(x - x_b\right)/\left(x_e - x_s\right)
\end{aligned}
\tag{4}
$$

Where $A = 0.2$ is the amplitude of the velocity disturbance, $w_g = 128$ is the period of adding disturbance. x_s is the location where the disturbance happened while x_e plays a opposite role.

3. DNS result: mean and instant properties

Figure 3 gives the Reynolds averaged velocity profile at incoming turbulent boundary layer. And figure 4 shows the dimensionless Reynolds stress distribution normalized by wall properties. From the figure 3, the distribution near the wall meets the wall's law while in the log-region the log –law has a good consistency with the numerical results. Significantly, intercept term of log-law 5.9

is larger than the situation in supersonic boundary layer, and the reason why causes the problem possibly is compressible effect due to high Mach number and strong nonlinear effect[10]. In figure 4, except streamwise normal Reynolds stress, others have a good fit with data in the references[11]. For the exception, it may be caused by the differences between plate and cylinder's spanwise surfaces[3]. In general, the result of incoming turbulent boundary layer explains the veracity of numerical simulation.

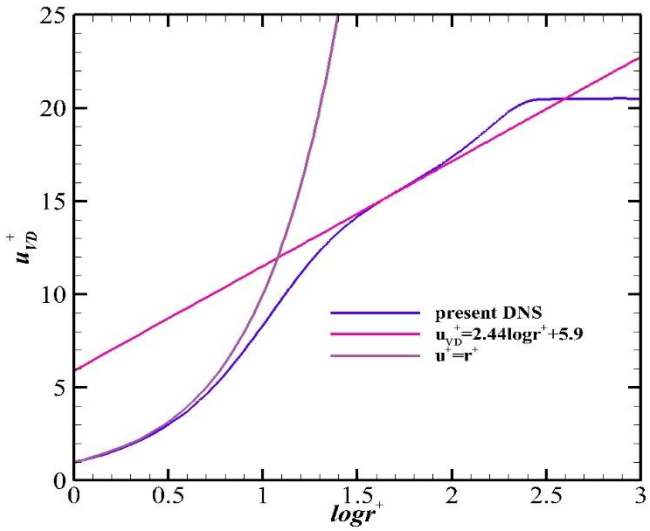

Figure 3 The averaged streamwise velocity profile at the incoming turbulent boundary layer

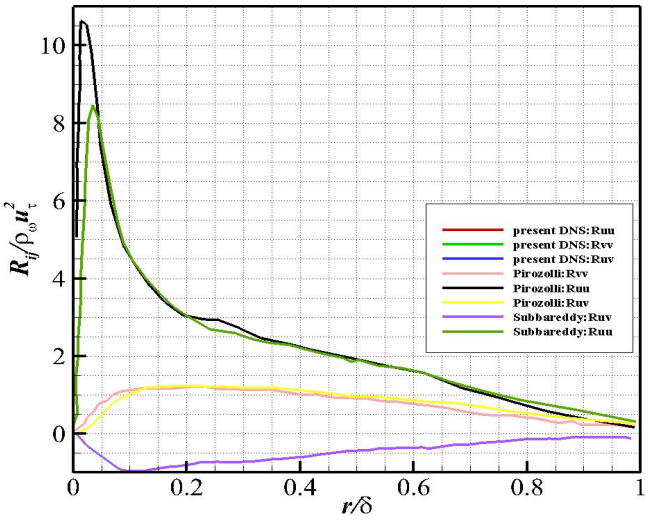

Figure 4 The distribution of Reynolds stress at the incoming turbulent boundary layer

The instantaneous vortical structures displayed by *Q* criterionare presented in Figure 5. The shock structure indicated in figure 6 as the density magnitude. And the furmula of Q criterion which can be indicated as:

$$Q_{cr} = \frac{1}{2}\left(|S|^2 - |\Omega|^2\right) \tag{5}$$

has been employed to identify the vortices extensively. The threshold value was adjusted to 0.01 to display the arc-like vortices near the interaction region. The figure indicated that after interaction the vortex structure performed various differences and varies rich experiences compared to the situation before interaction.

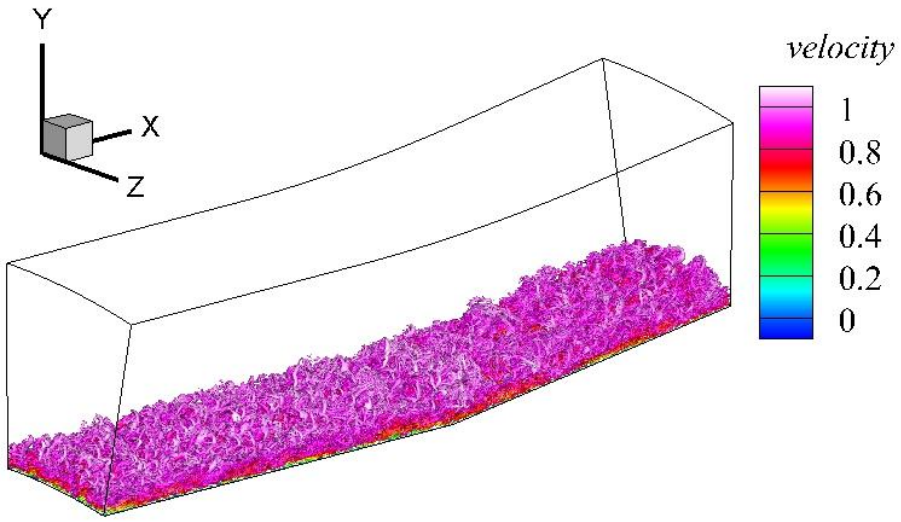

Figure 5 The iso-durface of Q colored by streamwise velocity and pressure gradient

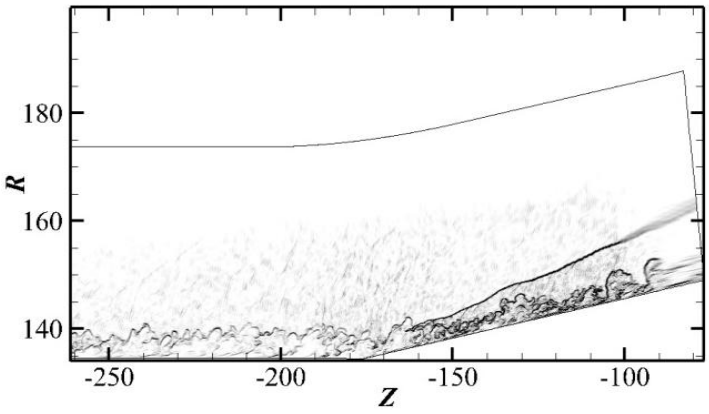

Figure 6 The density magnitude at the center plane near the interaction

Moreover, figure 7 shows the skin friction contour. And skin friction-pressure distribution along streamwise direction is shown in figure 8. In figure 7, the fact that three-dimensional effect in a 8.5 degree corner is not very obvious could be inferred from the situation that at interaction the corner do not have span wise Gortler vortexes due to small angles of corner. In addition to, the skin friction distribution meets the theoretical analysis' results such as Rankie-Hugoint relationship.

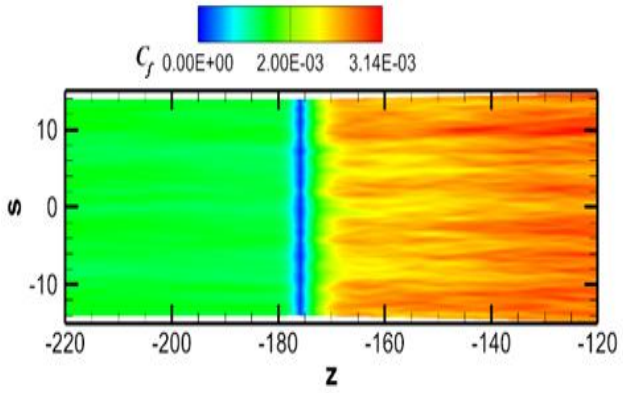

Figure 7 The contour of skin friction around the corner

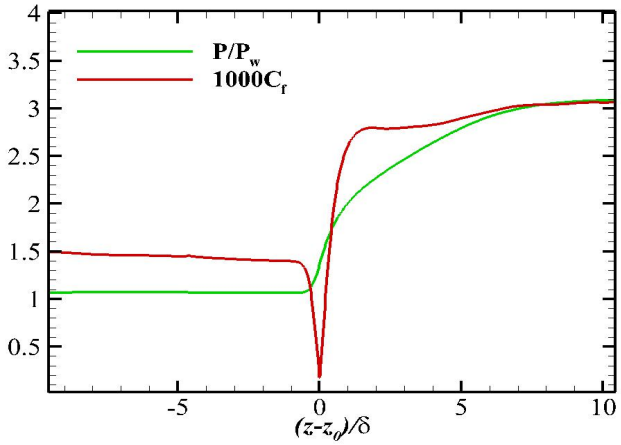

Figure 8 The distribution of skin friction and non-dimentional wall pressure along the streamwise direction

4. How to decompose skin friction in curved coordinate system

Basis on the investigation of the mean properties, in this section, we need to decompose skin friction to further study the mechanism of skin friction in curved coordinate system considering cylinder-flare configuration.

Favre averaged and Reynoldsaveraged properties could be written as following form,

$$\tilde{f} = \frac{\overline{\rho f}}{\overline{\rho}} \tag{6}$$

Considering averaged momentum equation and conservation law,

$$\begin{aligned} &\overline{\rho}\frac{\partial \tilde{u}}{\partial t} + \overline{\rho}\tilde{u}\frac{\partial \tilde{u}}{\partial x} + \overline{\rho}\tilde{v}\frac{\partial \tilde{u}}{\partial r} + \overline{\rho}\tilde{w}\frac{\partial \tilde{u}}{r\partial \theta} \\ &= -\frac{\partial \overline{p}}{\partial x} + \frac{\partial\left(\overline{\sigma_{11}} + \tau_{11}\right)}{\partial x} + \frac{\partial\left(\overline{\sigma_{12}} + \tau_{12}\right)}{\partial r} + \frac{\partial\left(\overline{\sigma_{13}} + \tau_{13}\right)}{r\partial \theta} + \frac{1}{r}\left(\overline{\sigma_{12}} + \tau_{12}\right) \end{aligned} \tag{7}$$

Where,

$$\begin{aligned}\tau_{11} &= -\left(\overline{\rho u^2} - \bar{\rho}\tilde{u}\tilde{u}\right)\\ \tau_{12} &= -\left(\overline{\rho uv} - \bar{\rho}\tilde{u}\tilde{v}\right)\\ \tau_{13} &= -\left(\overline{\rho uw} - \bar{\rho}\tilde{u}\tilde{w}\right)\end{aligned} \tag{8}$$

Transform absolute reference system to the wall reference system, we could obtain,

$$\begin{aligned}&\int_0^\delta \widetilde{u_a}\,\overline{\rho_a}\frac{\partial\widetilde{u_a}}{\partial t_a} + \overline{\rho_a}\widetilde{u_a}\widetilde{\left(u_a+u_\infty\right)}\frac{\partial\widetilde{\left(u_a+u_\infty\right)}}{\partial\left(x_a+u_\infty t\right)} + \overline{\rho_a v_a}\widetilde{u_a}\frac{\partial\widetilde{\left(u_a+u_\infty\right)}}{\partial r_a}\\ &+\overline{\rho_a}\widetilde{w_a}\widetilde{u_a}\frac{\partial}{r_a\partial\theta_a}\widetilde{\left(u_a+u_\infty\right)}dr_a = \int_0^\delta -\widetilde{u_a}\frac{\partial\overline{p}}{\partial\left(x_a+u_\infty t\right)}dr_a + \int_0^\delta\frac{\widetilde{u_a}}{r_a}\left(\overline{\sigma_{12}}+\tau_{12}\right)dr_a\\ &+\int_0^\delta\frac{\widetilde{u_a}}{r_a}\frac{\partial\left(\overline{\sigma_{13}}+\tau_{13}\right)}{\partial\theta_a}dr_a + \int_0^\delta\widetilde{u_a}\frac{\partial\left(\overline{\sigma_{11}}+\tau_{11}\right)}{\partial\left(x_a+u_\infty t\right)}dr_a + \int_0^\delta\widetilde{u_a}\frac{\partial\left(\overline{\sigma_{12}}+\tau_{12}\right)}{\partial r_a}dr_a\end{aligned} \tag{9}$$

Using the definition of skin friction and getting back to the initial reference system, the formula is,

$$\begin{aligned}C_f &= 2\int_o^\delta\left(\tilde{u}-1\right)\overline{\rho}\frac{D\tilde{u}}{Dt}dr + 2\int_0^\delta\left(\tilde{u}-1\right)\frac{\partial\overline{p}}{\partial x}dr\\ &-2\int_0^\delta\left(\tilde{u}-1\right)\frac{\partial\left(\frac{1}{\mathrm{Re}}\overline{\tau_{xx}} - \overline{\rho\widetilde{u''u''}}\right)}{\partial x}dr + 2\int_0^\delta\frac{\partial\left(\tilde{u}\right)}{\partial r}\left(\frac{1}{\mathrm{Re}}\overline{\tau_{xr}} - \overline{\rho\widetilde{u''v''}}\right)dr\\ &-2\int_0^\delta\left(\tilde{u}-1\right)\frac{1}{r}\frac{\partial\left(\frac{1}{\mathrm{Re}}\overline{\tau_{x\theta}} - \overline{\rho\widetilde{u''w''}}\right)}{\partial\theta}dr - 2\int_0^\delta\left(\tilde{u}-1\right)\frac{1}{r}\left(\frac{1}{\mathrm{Re}}\overline{\tau_{xr}} - \overline{\rho\widetilde{u''w''}}\right)dr\end{aligned} \tag{10}$$

Ignore the differences due to spanwise oscillators, the formula is,

$$\begin{aligned}C_{f\_2d} &= \underbrace{2\int_o^\delta\left(\tilde{u}\text{-}1\right)\overline{\rho}\frac{D\tilde{u}}{Dt}dr}_{Cf_1} + \underbrace{2\int_0^\delta\left(\tilde{u}-1\right)\frac{\partial\overline{p}}{\partial x}dr - 2\int_0^\delta\left(\tilde{u}-1\right)\frac{\partial\left(\frac{1}{\mathrm{Re}}\overline{\tau_{xx}} - \overline{\rho\widetilde{u''u''}}\right)}{\partial x}dr}_{Cf_2}\\ &\underbrace{-2\int_0^\delta\frac{\partial\left(\tilde{u}\right)}{\partial r}\frac{1}{\mathrm{Re}}\overline{\tau_{xr}}dr}_{Cf_3} \underbrace{-2\int_0^\delta\left(\tilde{u}-1\right)\frac{1}{r}\left(\frac{1}{\mathrm{Re}}\overline{\tau_{xr}} - \overline{\rho\widetilde{u''v''}}\right)dr}_{Cf_4} + \underbrace{2\int_0^\delta\frac{\partial\left(\tilde{u}\right)}{\partial r}\frac{1}{\mathrm{Re}}\overline{\rho\widetilde{u''v''}}dr}_{Cf_5}\end{aligned} \tag{11}$$

From (11), we concluded it by decompose skin friction into 5 parts:

Cf₁ stands for flow conduction and transport in turbulent boundary layer, *Cf₂* could be divided into three parts: pressure gradient item, normal Reynolds stress item and molecular viscous stress item. And *Cf₃* stands for molecular dissipation in turbulent boundary layer. *Cf₄* is the item due to coordinate's transform. Finally, *Cf₅* stands for the turbulent generation totally.

Table 1 performs the accuracy of skin friction decomposition. In table 1, except for *P₃*, reconstruct value have a good fit with initial value. For *P₃* (near shock interaction), the reason that unusual error appeared may be intermittent near interaction.

	P₁	*P₂*	*P₃*	*P₄*	*P₅*
Initial value（*10^3）	1.47	1.45	1.37	2.82	2.74
New value（*10^3）	1.49	1.47	1.52	2.92	2.78
Absolute error（*10^3）	0.02	0.02	0.15	0.10	0.04
Relative error（%）	1.71	1.30	9.87	3.42	1.44

5. Proper Orthogonal Decomposition

A proper orthogonal decomposition was used to analysis the pressure pulsation. Lumley et al. [11] carried out the method to study the turbulent flowfield. Here the formula of decomposition is given, exact details is located on the reference article[12].

$$U(x,y,z,t)=\overline{U}(x,y,z,t)+\sum_{i=1}^{n\_\mathrm{mod}} a_j(t)\phi(x,y,z) \tag{12}$$

We obtain eigenvalues of POD modes' distribution of Cf in figure 9. In figure 9, the POD modes decrease while energy modes increase. In figure 10, POD results shows the coefficient obey basically Gauss's distribution. And we could conclude that the astringency of mode's energy is as well as we expected

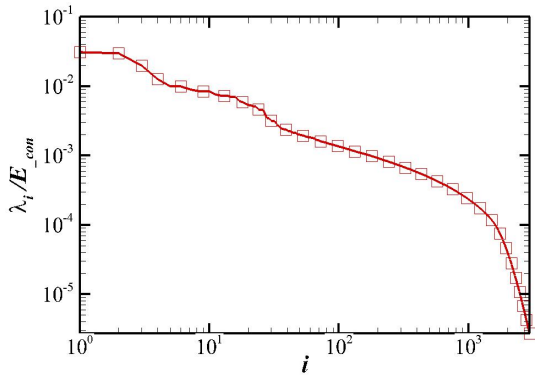

Figure 9 The distribution of eigenvalue along the POD modes of Cf

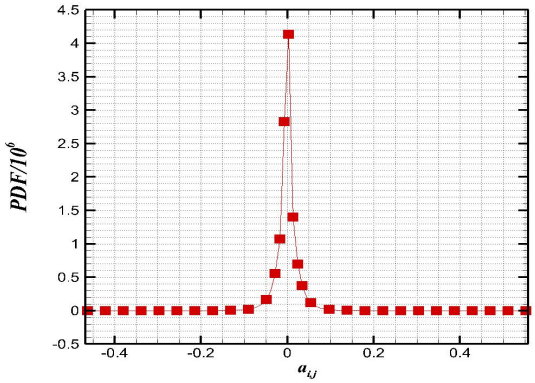

Figure 10 PDF of mode coefficients of Cf

The basic function $\phi(x,y,z)$ stands for the primary function in Hilbert space. To study $\phi(x,y,z)$, we reconstruct the function at x-z plane. And the mode number is 1,2,3,4,5,6,78,9,10,15,20,40,100 and 200 from the upper left picture to the bottom right one in figure 11. To compare the results of Cf and pressure to study the connection and differences of them, two pictures of them are given. Mode 1 stands for the main mode. And main mode's energy accounts for 20% of the total energy.

In figure 11, the quasi-steady "vortices" was founded in mode 1 which stands for the high pressure zones. From mode 2 to mode 10, the pressure stripe was indicated as the near wall's fluctuations, while the mode in mode 11 to mode 15 becomes more and more fragmented. By contrast , the Cf mode indicates almost unchanged features where streamwise stripes covered the dominant zone from mode1 to mode 14, and in mode 15, the features changed which indicated as fragmented stripes. Compare the results of Cf and pressure, the energy in the zone varies different features but in the interaction zone, the features become almost the same as the original one.

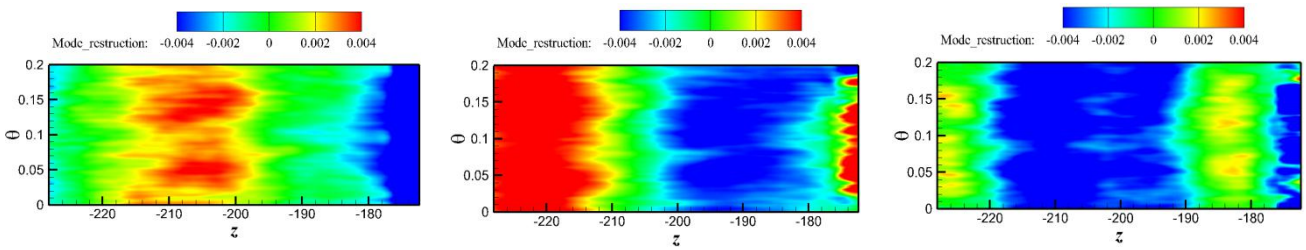

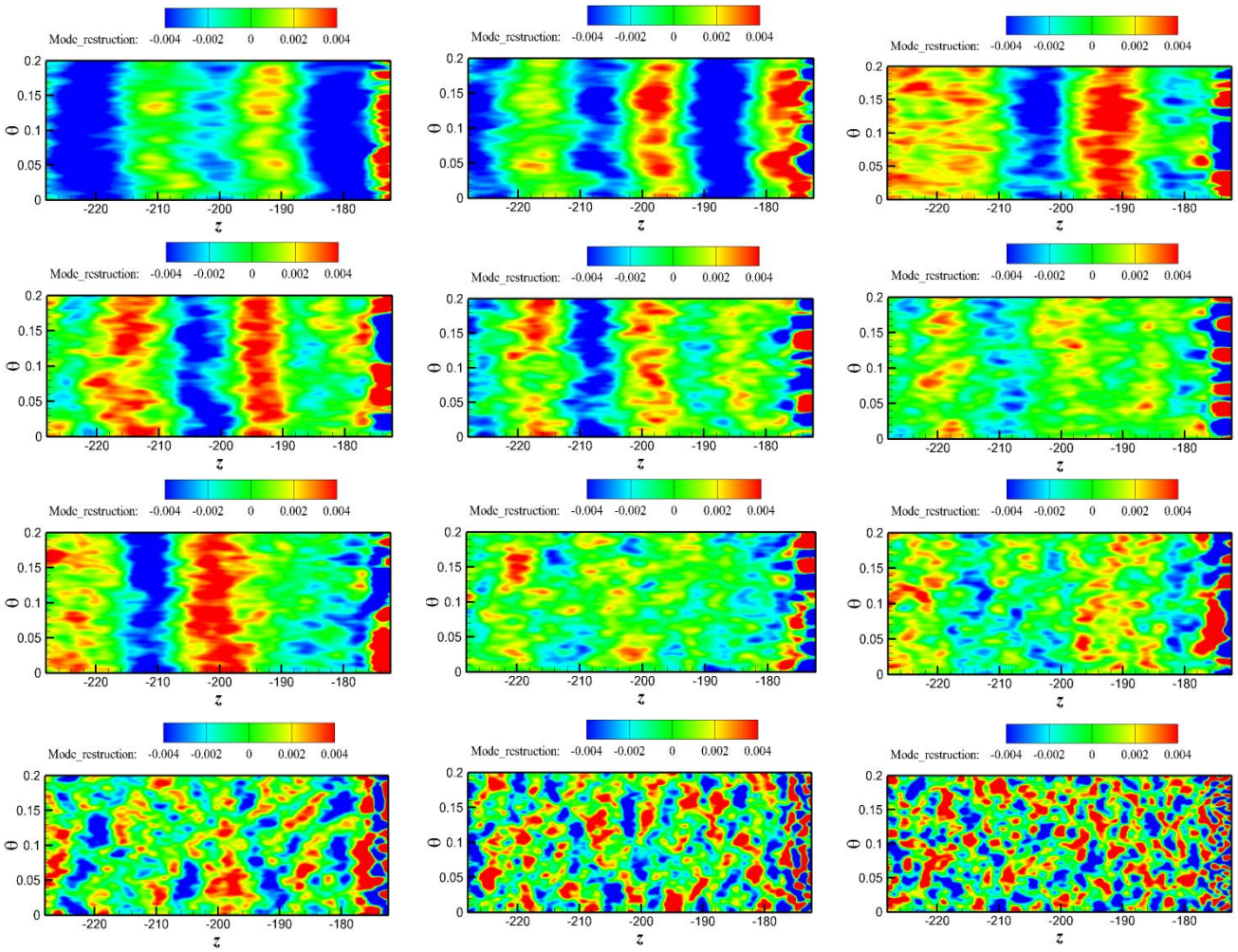

Figure 11 Mode coefficient distribution of pressure

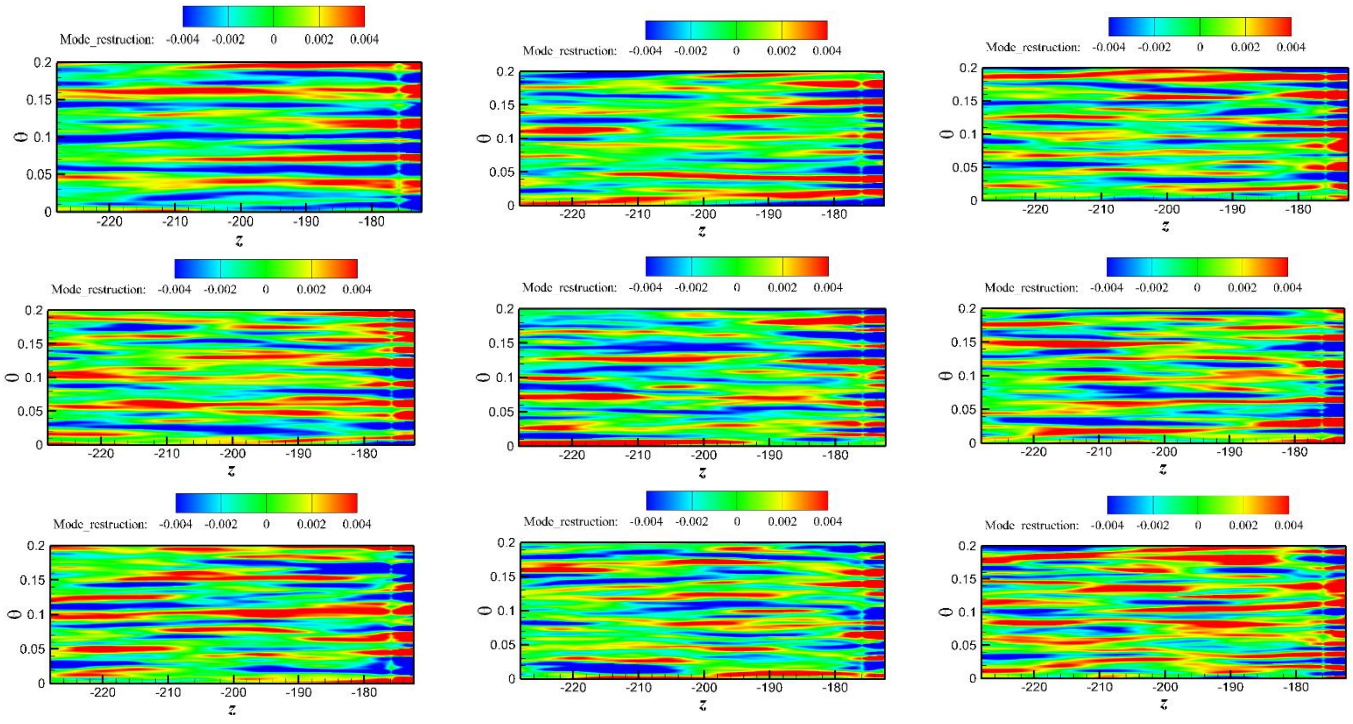

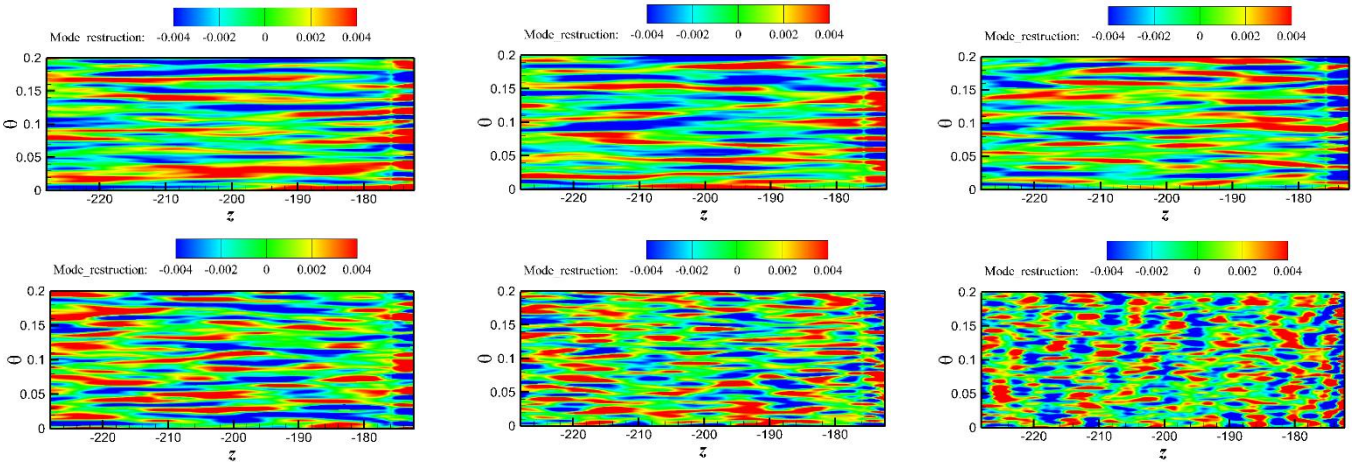

Figure 12 Mode coefficient distribution of Cf

6. Conclusion and Summary

The present work mainly focuses on the skin friction of SWBTLI in a hollow cylinder-flare configuration at Mach 6 using direct numerical simulation. The exact structures of coherent vortices and statistical properties have been obtained. On the basis of the flowfield data, the formula of decomposition into 5 parts: convection, turbulent dissipation, viscous dissipation, streamwise heterogeneous quality and extra part due to coordinate system transformation using the formula. Moreover, to study the unsteady properties of the flowfield, the proper orthogonal decomposition method was used to decompose the pressure pulsation. POD results indicate that modes of Cf and pressure indicates different features expect for the interaction zone, where the features becomes same as the original one.

7. Contact Author Email Address

corresponding@ yuanxianxu@cardc.cn.

8. Copyright Statement

Acknowledgments

This work is supported by the (2019YFA0405300), National Natural Science Foundation of China (Grant Number: 11802324) and National Numerical Windtunnel project.

References

[1] Ferri, A., “Experimental Results with Airfoils Tested in the High Speed Tunnel at Guidonia,” (translation). 1940, NACA TM 946.

[2] BOOKEY P, WYCKHAM C, SMITS A. Experimental investigations of Mach 3 shock-wave turbulent boundary layer interactions[C].2005, AIAA 2005-4899.

[3] 孙东，刘朋欣，童福林. 展向振荡对激波/湍流边界层干扰的影响研究[J]. 航空学报, 2021, 42(1): 12405.

[4] FUKAGATA, K., IWAMOTO, K. & KASAGI, N. Contribution of Reynolds stress distribution to the skin friction in wall-bounded flows. Phys. Fluids, 2002, 14 (11), 73–76.

[5] Sébastien Deck, Nicolas Renard. A theoretical decomposition of mean skin friction generation into physical phenomena across the boundary layer[J]. J. Fluid Mech. 2016, 790, 339–367.

[6] Sung HJ, Yoon M, Hwang J. Contribution of large-scale motions to the skin froction in amoderate adverse pressure gradient turbulent boundary layer[J]. J Fluid Mech. 2018, 848: 288-311.

[7] Yoon M, Hwang J, Sung HJ. Contribution of velocity-vorticity correlations to the frictional drag in wall-bounded turbulent flows. Phys. Fluids, 2016(b), 28(8), 081702.

[8] 李新亮，傅德熏，马延文. 可压缩尖锥边界层转捩的直接数值模拟[J]. 中国科学, 2008, 38(1): 1-13.

[9] LI X L, LENG Y, HE Z W, Optimized sixth-order mononicity-preserving scheme by nonlinear spectral analysis. International Journal For Numerical Methods In Fluids, 2013; 73: 560-577.

[10] 傅德熏， 马延文，李新亮. 可压缩湍流直接数值模拟[M]. 北京：科学出版社， 2010.

[11] Pirozzoli S, Grasso F. Direct numerical simulation of impinging shock wave/turbulent boundary layer interaction at M=2.25[J]. Phys. Fluids, 2006, 18:065-113.

[12] Gal Berkooz, Philip Holmes, and John L. Lumley. The proper orthogonal decomposition in the analysis of turbulent flow[J]. Annu. Rev. Fluid Mech. 1993.25: 539-75.